Calibration of 2D Thermal Simulations for Large-Scale Additive Manufacturing Using Thermography Maps

H. Courteau-Godmaire[1*], N. Courion[2], and P. Hubert[2]

[1] Composites Technical Center, Hutchinson S.A., Montreal, Canada, [2] Department of Mechanical Engineering, McGill University, Montreal, Canada

* *Corresponding author (hubert.courteau-godmaire@hutchinson.com)*

Keywords: *Additive manufacturing; heat transfer simulation; process modelling; thermography*

1. Abstract

Large-scale additive manufacturing of thermoplastic composites requires accurate thermal control to ensure dimensional stability and strong interlayer bonding. Previous experimental work has demonstrated the critical impact of thermal history. Building on this foundation, the present study develops a fast and flexible numerical model to simulate temperature evolution during the process.

Experiments were conducted on a vertical wall printed in carbon fiber-reinforced polycarbonate. Surface temperature was measured using an infrared camera. The data were used to calibrate a 2D transient finite element model implemented in MATLAB. An optimization algorithm was applied to identify physical parameters, including the heat transfer coefficient and thermal conductivity. The parameters were fitted simultaneously across eight print setting variations.

The model reproduces the main thermal trends with good agreement, particularly for bulk cooling. Larger discrepancies are observed near the deposition front and during the first few layers. The optimized conductivity shows low variability across different calibration regions (bulk cooling or deposited layers). This indicates that conductivity acts as an effective parameter while still enabling accurate thermal predictions.

Overall, the framework provides a fast and flexible tool for exploring thermal behavior in large-scale additive manufacturing and highlights key limitations and directions for improving physical modelling.

2. Introduction

Large-scale additive manufacturing of thermoplastic composites is used for the rapid fabrication of tooling in the composite industry. The thermal history experienced during deposition is a primary factor governing interlayer bonding and final part performance. Accurate characterization and prediction of temperature evolution during printing are therefore essential for process understanding and optimization.

Recent experimental work performed by Courion in collaboration with Hutchinson, as part of his master's thesis [1], provided clear insight into the role of thermal history in interlayer adhesion for carbon reinforced polycarbonate. Through controlled printing experiments, infrared thermography, mechanical testing, and fractography, his work confirmed that layer time governs the thermal window available for interlayer healing. Short layer times enhance interlayer diffusion above *Tg* but can cause wall sag, while long layer times promote cooling and brittle behavior.

The clarity of the experimental results and the simplicity of the printed geometry naturally motivated the development of a complementary numerical model. A thermal model enables exploration of internal temperature fields that cannot be accessed experimentally and allows the influence of individual parameters to be isolated. Ultimately, such a model could support a transition from post-test interpretation to predictive control of printing conditions.

Thermal simulation of large-scale additive manufacturing is well established, with significant prior contributions from the Purdue University LSAM research laboratory [2–4]. The simulation work presented in this paper follows a different objective, focusing not on high-fidelity reproduction but on the development of a transparent, flexible, and computationally efficient framework for systematic parameter exploration.

Accordingly, this work presents a two-dimensional transient finite element model calibrated with experimental thermal maps. The experimental methodology, numerical formulation, calibration strategy, and results are presented sequentially, followed by a discussion of limitations and perspectives.

3. Experimental Methods

An overview of the experimental configuration and the corresponding simulation domain is shown in Figure 1, while a photograph of the experimental setup is provided in Figure 2

3.1. Material and Printing System

The experiments were conducted using a polycarbonate matrix reinforced with 20 wt.% short carbon fibers (DAHLTRAM C-250CF, Airtech), a material commonly used for large-scale additive manufacturing of composite tooling. Printing was performed on a Thermwood Multipurpose 90 system equipped with a custom pellet-fed single-screw extruder. A nozzle diameter of 7 mm was used, and the extrusion temperature was set to 320 °C for all experiments.

Specimens were printed on either a 5/8-inch-thick borosilicate glass substrate (Pyrex) or a ceramic insulation substrate. Between successive experimental runs, the Pyrex substrate was cooled in tap water to ensure a repeatable and uniform initial temperature condition prior to each print. The ceramic substrate was cooled using a compressed-air gun.

3.2. Printed Geometry and Deposition Strategy

The printed specimen consisted of a 60 mm tall vertical wall, formed by two adjacent beads per layer. Each bead had a nominal width of 10 mm and a thickness of 2.5 mm, resulting in a total wall thickness of 20 mm. Each layer consisted of depositing one bead along the wall length, shifting laterally by one bead width, and depositing the adjacent bead along the return path. A prescribed dwell time was imposed between successive layer depositions.

The wall geometry was chosen such that its length is large compared to its thickness and height, resulting in negligible temperature gradients along the longitudinal direction. Consequently, the thermal behavior can be accurately represented using a two-dimensional cross-sectional model.

Three interlayer dwell times were investigated: 45 s, 60 s, and 90 s. To assess the influence of convective cooling on the thermal history, two convection configurations were considered: natural convection with no forced airflow, and forced convection generated by a small fan positioned at 3 ft from the wall (~between 1 and 2 m/s flow). Dwell time and airflow variations were conducted on either the Pyrex or the ceramic substrate. The full experimental matrix is shown in Table 1.

Table 1. Experimental matrix.

	Run 1	Run 2	Run 3	Run 4	Run 5	Run 6	Run 7	Run 8
Dwell time	60 s	60 s	45 s	90 s	90 s	60 s	60 s	45 s
Convection	natural	3 ft fan	3 ft fan	natural	natural	3 ft fan	natural	3 ft fan
Substrate	**Pyrex**	**Pyrex**	**Pyrex**	**Pyrex**	ceramic	ceramic	ceramic	ceramic

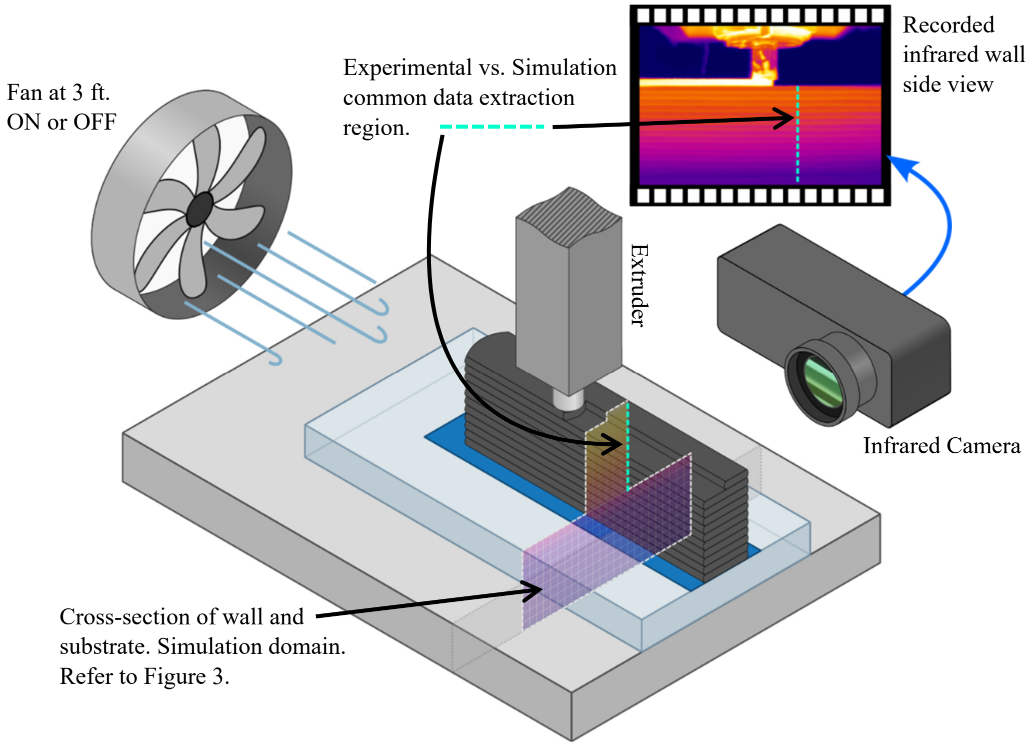

Figure 1. Overview of the experimental configuration and numerical modelling domain, including the printed wall and substrate, convection conditions, infrared acquisition, and vertical data extraction line used for thermal map extraction and comparison.

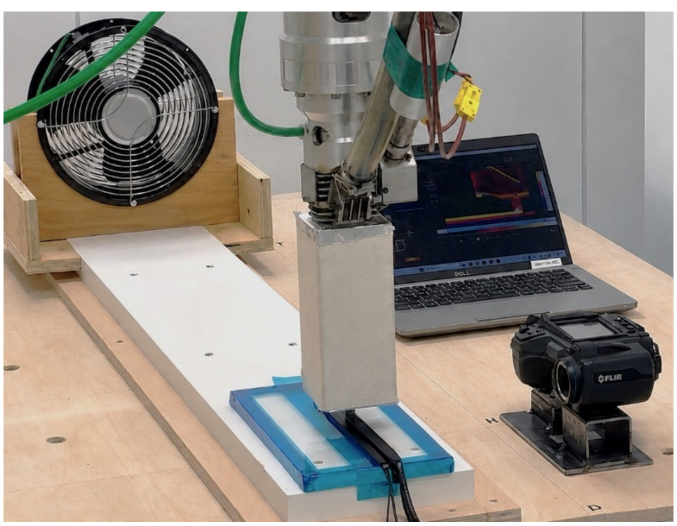

Figure 2. Photograph of the experimental setup corresponding to the schematic shown in Figure 1. (cabling removed with AI)

3.3. Thermal Measurements

Thermal evolution during printing was monitored using a laterally positioned infrared camera. Time-resolved radiometric data were recorded and processed to extract surface temperature fields.

For each frame, a vertical pixel line at the center of the field of view (Figure 1) was extracted and arranged side by side in time to form a two-dimensional thermal map (Figure 4), with time and wall height as axes. This representation captures the transient thermal history along the build height and serves as the basis for comparison with numerical simulations.

4. Numerical Methods

The methodology builds on Whokko [5], extending the approach from 1D to 2D. The model represents a 2D cross-section of the printed wall and substrate, assuming negligible variation along the printing direction (out of plane). The simulation domain is presented in Figure 3.

4.1. Governing Equation and Weak Form

The transient heat transfer problem is governed by the heat equation in the absence of internal volumetric heat generation. In strong form, the governing equation reads:

$$\rho c \frac{\partial T}{\partial t} = \nabla \cdot (k \nabla T) \tag{1}$$

where T is the temperature field, ρ is the material density, c is the specific heat capacity, k is the thermal conductivity, t is time. Heat losses due to convection and radiation occur at the boundaries and are introduced later through boundary conditions.

To derive the finite element formulation, the weak form of the heat equation is defined as follows:

$$\int_\Omega \rho c \, \delta T \frac{\partial T}{\partial t} \, d\Omega + \int_\Omega \nabla \delta T \cdot k \nabla T \, d\Omega = \int_\Gamma \delta T \, q \, d\Gamma \tag{2}$$

where Ω is the spatial domain, δT is an admissible test function, Γ denotes the boundary surface, and q represents the heat transfer through the surface.

4.2. Finite Element Approximation

The temperature field and the test function are approximated in 2D using standard finite element interpolation as:

$$T(x,y) \approx \mathbf{N}(x,y)\mathbf{T}, \qquad \delta T(x,y) \approx \mathbf{N}(x,y)\delta\mathbf{T}, \tag{3}$$

where **N** is the vector of shape functions and **T** is the vector of nodal temperatures.

For convenience, bilinear quadrilateral shape functions are defined directly in the physical coordinate space of each element. For a rectangular element of width a and height b, the shape functions are written as:

$$\begin{aligned} N_1 &= \frac{1}{ab}\left(\frac{a}{2} - x\right)\left(\frac{b}{2} - y\right), \qquad N_2 = \frac{1}{ab}\left(\frac{a}{2} + x\right)\left(\frac{b}{2} - y\right), \\ N_3 &= \frac{1}{ab}\left(\frac{a}{2} + x\right)\left(\frac{b}{2} + y\right), \qquad N_4 = \frac{1}{ab}\left(\frac{a}{2} - x\right)\left(\frac{b}{2} + y\right), \end{aligned} \tag{4}$$

The temperature gradient within an element is expressed as:

$$\nabla T = \mathbf{B}\,\mathbf{T} \tag{5}$$

where the gradient operator $\mathbf{B}$ is defined by

$$\mathbf{B} = \begin{bmatrix} \dfrac{\partial N_1}{\partial x} & \dfrac{\partial N_2}{\partial x} & \dfrac{\partial N_3}{\partial x} & \dfrac{\partial N_4}{\partial x} \\ \dfrac{\partial N_1}{\partial y} & \dfrac{\partial N_2}{\partial y} & \dfrac{\partial N_3}{\partial y} & \dfrac{\partial N_4}{\partial y} \end{bmatrix} \tag{6}$$

Substituting the finite element interpolations of the temperature field and test function into the weak form given in Eq. (2) leads to the definition of the thermal capacity matrix $\mathbf{C}$, the conductivity matrix $\mathbf{K}$ and the heat flux vector $\mathbf{f}$:

$$\mathbf{C} = \int_\Omega \rho c\, \mathbf{N}^T\mathbf{N}\, d\Omega\ , \qquad \mathbf{K} = \int_\Omega \mathbf{B}^T k \mathbf{B}\, d\Omega\ , \qquad \mathbf{f} = \int_\Gamma \mathbf{N}^T q\, d\Gamma \tag{7}$$

Using these definitions, the spatially discretized form of the governing equation is written as:

$$\mathbf{C}\dot{\mathbf{T}} + \mathbf{K}\mathbf{T} = \mathbf{f} \tag{8}$$

To solve this system in time, an implicit generalized θ-method is employed. Over a time increment Δt between time steps t^n and t^{n+1}, the compact form of Eq. (8) leads to the time-discrete form:

$$\underbrace{\left(\frac{\mathbf{C}}{\Delta t} + \theta\mathbf{K}\right)}_{\mathbf{K}^*}\mathbf{T}^{n+1} = \underbrace{\left(\frac{\mathbf{C}}{\Delta t} - (1-\theta)\mathbf{K}\right)\mathbf{T}^n + \mathbf{f}}_{\mathbf{f}^*} \tag{9}$$

Here, θ is the time-integration parameter, restricted between 0.5 and 1.0 to ensure stability. All terms on the right-hand side are known at time level t^n, and the only unknown is the temperature vector $\mathbf{T}^{n+1}$. For convenience, this new system is written in the compact form:

$$\mathbf{K}^*\mathbf{T}^{n+1} = \mathbf{f}^* \tag{10}$$

which represents a linear system solved at each time step to advance the temperature field in time.

4.3. Boundary Conditions

Boundary heat losses are incorporated through the heat-flux vector $\mathbf{f}$ and additional contributions to the conductivity matrix $\mathbf{K}$. Convective heat transfer is modeled using Newton's law:

$$q_{conv} = h(T - T_\infty) \tag{11}$$

where h is the convection coefficient and T_∞ is the ambient temperature. The contribution of hT is assembled into $\mathbf{K}$, while the term proportional to hT_∞ contributes to $\mathbf{f}$.

Radiative heat transfer at the surface is modeled using the Stefan–Boltzmann law,

$$q_{rad} = \varepsilon\sigma(T^4 - T_\infty^4) \tag{12}$$

where ε is the surface emissivity and σ is the Stefan–Boltzmann constant. To retain a linear system at each time step, the term T^4 is linearized about a reference temperature $\bar{T}$, taken as the average temperature along the considered boundary edge. The first-order Taylor expansion yields:

$$q_{rad} \approx \underbrace{4\varepsilon\sigma\bar{T}^3 T}_{temparture-dependent} - \underbrace{\varepsilon\sigma(3\bar{T}^4 + T_\infty^4)}_{constant\ term} \tag{13}$$

The temperature-dependent term is assembled into the conductivity matrix $\mathbf{K}$, while the constant term contributes to the heat-flux vector $\mathbf{f}$.

4.4. Solution Algorithm

The transient thermal problem is solved using a layer-by-layer strategy that mirrors the additive manufacturing process. At the beginning of each layer deposition step, the computational domain is updated to reflect material deposition. A dedicated mesh-connectivity function is used to regenerate the new element connectivity and to identify the node regions associated with boundary surfaces. The temperature field is then advanced in time. The simulation of a complete print is performed in approximately 2 seconds, enabling rapid parameter calibration and exploration.

The overall procedure is summarized as follows:

1. Activate the new layer by adding elements. Update connectivity. Identify boundary nodes.
2. Initialize the temperature field by retaining existing nodal temperatures and assigning the nozzle temperature to new nodes.
3. Reassemble the global conduction matrix $\mathbf{K}$ and capacity matrix $\mathbf{C}$ for the updated domain.
4. Apply convective (Figure 3) and radiative (all exposed surfaces) boundary conditions on boundary nodes, assembling contributions into $\mathbf{K}$ and the heat-flux vector $\mathbf{f}$.
5. Advance the solution in time by solving the implicit θ-method system. For efficiency, the time step increases progressively and is reset at each new layer activation.
6. Store the updated temperatures and repeat until completion of all layers.

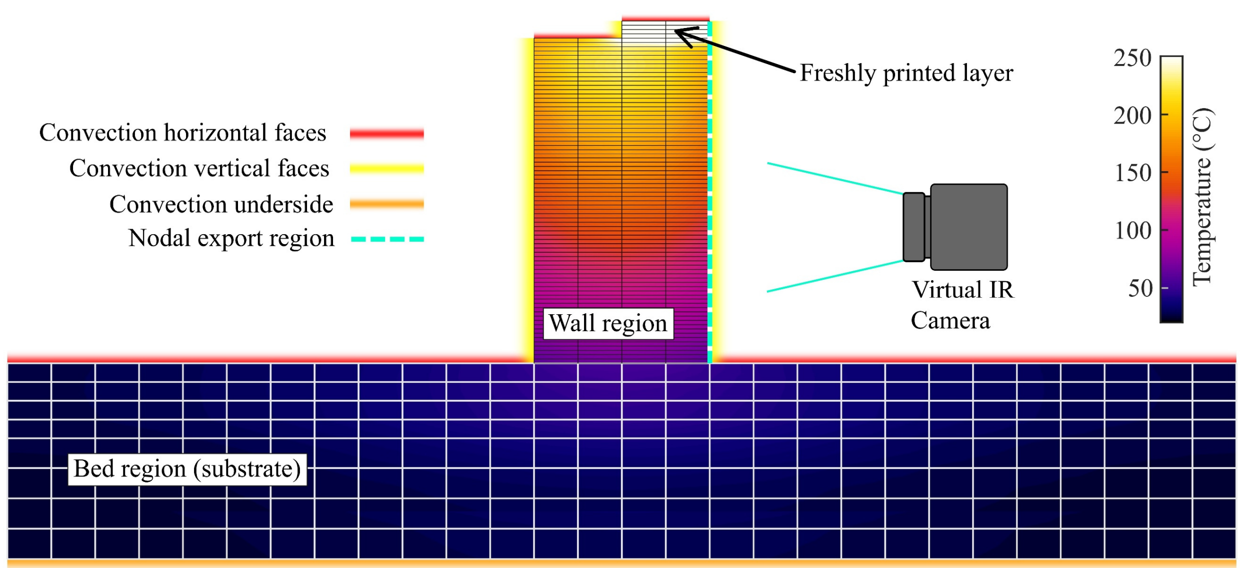

Figure 3. 2D simulation domain with bed and wall regions. Printing direction through the page. Convective boundary conditions definition.

5. Model Calibration

5.1. Material properties

The material properties are presented in Table 2 followed by their references:

Table 2. Material Properties.

Material	Density [kg/m³]	Heat Capacity [J/(kg·K)]	Thermal Conductivity [W/(m·K)]
DAHLTRAM C-250CF	1110 [1] (1210 [2])	1200 [3]	0.41 (0.372 to 0.470) [4]
Borosilicate (direct substrate)	2230 [5]	830 [5]	1.2 [5]
Plywood (bed)	650 [6]	1500 [7]	0.12 [7]
Ceramic BNZ CS85 (bed)	1362 [8]	1000 [9]	0.31 [8]

[1]Measured on printed parts with Archimedes' principle. ASTM D792.
[2]Dahltram® C-250CF Technical Data Sheet.
[3]Taken from [1] as an estimated value. Known to be variable w.r.t temperature.
[4]Average and (range) obtained experimentally with C-Therm TCi Thermal Conductivity Analyzer. Isotropy is assumed.
[5]www.mcmaster.com/8476K78-8476K787/ – BOROFLOAT® 33 – Thermal Properties.
[6]Measured: mass over volume of a slab.
[7]Taken from https://materials.fsri.org/materialdetail/plywood
[8]Taken from www.bnzmaterials.com/structural-insulation/cs85/
[9]Estimated from Promat MONALITE-M1T (similar to CS85).

5.2. Thermal Map Processing

To ensure a consistent comparison between experimental and numerical results, both datasets were processed to lie on a common spatial and temporal grid. Experimental thermal maps were resampled and mildly smoothed. Alignment was achieved by matching the staircase features shown in Figure 4, ensuring that corresponding layer transitions coincided in time and height in both datasets.

The flat portions at the top of each step in the experimental maps were trimmed prior to comparison. This step mitigates halo and blur artifacts observed near sharp temperature transitions between freshly deposited material and the background.

5.3. Multi-Case Optimization

Model calibration was performed using the Covariance Matrix Adaptation Evolution Strategy (CMAES) optimization algorithm. The calibration function was defined as the minimization of the sum of squared error between experimentally measured and numerically predicted thermal maps. The global objective function corresponds to the sum of squared error accumulated over all eight experimental runs, such that a single parameter set was calibrated to reproduce the entire dataset.

The primary parameters optimized during calibration were:

- Convection coefficients applied to vertical surfaces,
- Convection coefficients applied to horizontal surfaces,
- Thermal conductivity of the printed material,
- Thermal contact resistance between the printed wall and the substrate,
- Convective heat transfer at the underside of the build platform,
- Initial substrate (bed) temperature.

Calibration was performed using a series of three independent optimization cases. Each case targeted a specific subset of the thermal history map in order to assess parameter sensitivity:

- **Upper half of the build**, exclude early layers to minimize the influence of substrate and interface effects and primarily capture bulk heat transfer within the wall
- **Full thermal map,** allow the influence of substrate temperature and interface resistance.
- **A diagonal band** (250 s wide) along the layer-by-layer **deposition front**, emphasize transient reheating associated with newly deposited material

Each optimization case was repeated six times using different random initializations within the parameter bounds to assess the robustness of the identified solution.

These optimization studies were conducted independently and did not constrain or inform each other. However, prior use of the model provided guidance for defining physically realistic bounds for each parameter shown in Table 3. All parameters were therefore optimized within prescribed ranges reflecting expected material behavior and plausible heat-transfer conditions.

6. Results and Discussion

The optimized parameters obtained from the three calibration subsets are summarized in Table 3. Thermal conductivity and forced convection coefficients exhibit low variability across all cases and are well constrained. In contrast, substrate temperature and underside convection show high variability, reflecting their indirect influence on the wall temperature field and limited observability from surface measurements.

Table 3. Optimized parameters for the three calibration subsets. Values represent averages across repeated runs. Bold: low variability (≤ 3%); italic: moderate variability (3–10%); red: high variability (> 10%).

Parameter		Thermal Conduct.	Interface Resist.	HTC Vertical Natural	HTC Vertical Fan	HTC Flat Natural	HTC Flat Fan	Bed T° Ceramic	Bed T° Pyrex	HTC Under-side
units		W/(mK)	m^{2}K/W	W/m^{2}K	W/m^{2}K	W/m^{2}K	W/m^{2}K	°C	°C	W/m^{2}K
Lower bound		0.22	$10^{-3.0}$	0.8	5.0	2.0	22.0	30.0	20.0	0.0
Upper bound		0.35	$10^{-4.5}$	3.0	9.0	4.0	35.0	45.0	35.0	30.0
Optimized	Top	**0.261**	*$10^{-3.2}$*	**0.81**	**5.4**	**3.3**	**34.5**	35.4	27.0	24.1
	Full	**0.336**	**$10^{-4.2}$**	*2.12*	**5.7**	*2.2*	**34.1**	37.2	28.3	*4.8*
	Stair	**0.339**	**$10^{-4.1}$**	**0.84**	**5.6**	*3.7*	**35.0**	36.2	25.4	11.8

A redistribution of parameters is observed across calibration subsets. When only the upper layers are considered, the optimized thermal conductivity is lower, while inclusion of the full thermal map leads to a systematic increase. In all cases, the variability remains low, indicating that conductivity is consistently constrained by the calibration.

However, the conductivity values differ between cases and from experimental measurements. This shows that conductivity does not act purely as a material property but compensates for model limitations, including simplified boundary conditions, interface behavior, and geometry. As a result, it behaves as an effective parameter used to match the overall thermal response.

Convection plays a dominant role in the thermal behavior. Forced convection is consistently identified with low variability, indicating a well-defined level of heat removal. In contrast, natural convection shows higher variability, reflecting interaction with radiation and substrate conduction. This suggests that the simplified boundary condition representation limits the ability to separate these effects.

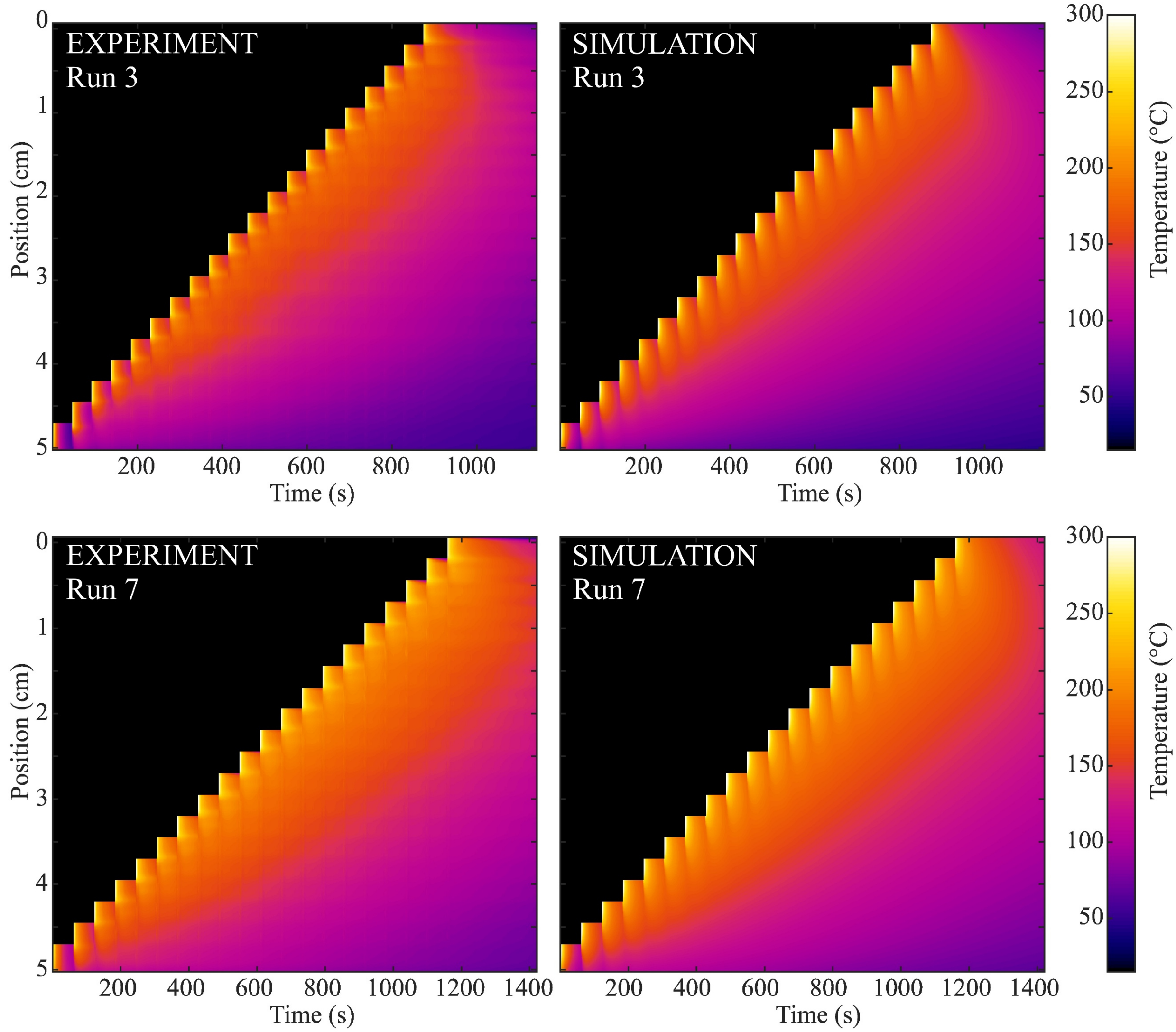

Figure 4. Comparison of experimental and simulated thermal maps for Run 3 and Run 7

In Figure 4, the model reproduces the experimental thermal maps well, particularly for bulk cooling behavior. Larger discrepancies are observed in the early layers and near the deposition front, where reheating is overestimated. These differences are partly attributed to geometric simplifications, as the experimental wall exhibits a bead-scale texture not captured in the model.

The similarity between full-map and staircase-only optimizations can be explained by the definition of the objective function. Because the calibration minimizes the sum of squared error, regions with larger discrepancies dominate the solution, particularly along the staircase “steps”. As a result, both approaches focus on these regions and produce comparable parameter sets.

7. Conclusion

A two-dimensional transient thermal model was developed and calibrated using infrared thermal maps for large-scale additive manufacturing of carbon fiber-reinforced polycarbonate. The model accurately captures the dominant thermal behavior, particularly bulk cooling, while remaining computationally efficient (~2 seconds per run) and straightforward to implement.

The calibration results show that some parameters, such as thermal conductivity and forced convection, are strongly constrained, while others remain weakly identifiable due to their indirect influence on surface temperature measurements. In particular, thermal conductivity behaves as an effective parameter, compensating for modelling simplifications rather than representing a uniquely identifiable material property.

The observed discrepancies, especially near the deposition front and during early layer cooling, highlight limitations in the current physical representation. These include simplified boundary conditions, approximate interface behavior, idealized geometry, and uncertainties in the experimental measurements.

A key strength of the present approach lies in its flexibility. The MATLAB implementation allows straightforward introduction of parameter dependencies, such as temperature-dependent properties or spatially varying boundary conditions. This makes it possible to progressively refine the physical description of the process and directly improve the model as new insights are gained.

Overall, the framework provides a practical tool for bridging experimental observations and numerical modelling, while clearly identifying the limits of current assumptions. The flexibility of the approach makes it well suited for systematically improving the representation of heat transfer and extending the model toward more predictive capabilities.

The code and framework can be shared upon request to support further use and development. The approach provides a practical basis for improving the physical description of heat transfer and advancing understanding in large-scale additive manufacturing.

8. References

[1] N. Courion. "*Improving interlayer adhesion in large-scale additive manufacturing for composite tooling*". Thesis, McGill University, 2026.
[2] B. Brenken, A. Favaloro, E. Barocio, N.M. DeNardo and R.B. Pipes. "Development of a model to predict temperature history and crystallization behavior of 3D printed parts made from fiber-reinforced thermoplastic polymers". *Proceedings of the SAMPE Conference*, p. 704, 2016.
[3] A. Favaloro, B. Brenken, E. Barocio and R.B. Pipes. "Simulation of polymeric composites additive manufacturing using Abaqus". *Proceedings of Science in the Age of Experience*, pp 103-114, 2017.
[4] B. Brenken, E. Barocio, A. Favaloro, V. Kunc and R.B. Pipes. "Development and validation of extrusion deposition additive manufacturing process simulations". *Additive Manufacturing*, Vol. 25, pp 218-226, 2019.
[5] S. Whokko. "*Finite Element Method for 1D Transient Convective Heat Transfer Problems*". Thesis, 2018.